Petroleum Science 23 (2026) 5049–5062

Contents lists available at ScienceDirect

Petroleum Science

journal homepage: www.keaipublishing.com/en/journals/petroleum-science

Original Paper

3-D contour inversion of pipeline defects based on direction-aware multi-axis fusion and depth-gradient joint decoding

Lu-Shuai Xu [a,c], Shao-Hua Dong [a,b,c,*], Feng Li [d], Hao-Tian Wei [b,c], Cong Zuo [e], Di Qian [f], Peng Hou [g]

[a] College of Artificial Intelligence, China University of Petroleum (Beijing), Beijing, 102249, China
[b] College of Safety and Ocean Engineering, China University of Petroleum (Beijing), Beijing, 102249, China
[c] Key Laboratory of Oil and Gas Safety and Emergency Technology, Ministry of Emergency Management, Beijing, 102249, China
[d] PipeChina Beijing Pipeline Co., Ltd., Beijing, 100020, China
[e] Zhongke Zhiyu (Shouguang) Safety Technology Co., Ltd., Shouguang, 262700, Shandong, China
[f] High Pressure Pipe Network Branch, Beijing Gas Group Co., Ltd., Beijing, 100011, China
[g] PipeChina North Pipeline Co.Ltd., Beijing, 100011, China

ARTICLE INFO

Article history:
Received 2 December 2025
Received in revised form
24 February 2026
Accepted 17 March 2026
Available online 20 March 2026

Edited by Meng-Jiao Zhou

Keywords:
Oil and gas pipeline
Magnetic flux leakage internal inspection
Signal processing
3-D contour
Defect inversion

ABSTRACT

Reconstructing defect contours by inspecting internal magnetic flux leakage (MFL) in oil and gas pipelines provides significant data support for assessing pipeline integrity and represents a crucial step in MFL data analysis. Traditional methods often suffer from blurred edges and low structural similarity in multiple reconstructed images, making them inadequate for high-precision inspection. This paper proposes a three-dimensional (3-D) pipeline defect contour inversion method based on direction-aware multi-axis fusion and depth-gradient joint decoding (MFL-MAARN), which enhanced feature representation by fusing MFL signals with coordinate information. This work also designed a deep network architecture that combined a residual module with an attention gate mechanism and constructed a composite loss function combining MAE and the structural similarity index (SSIM). This achieved dual optimization aimed at both 3-D defect contour detail recovery and global structural reconstruction. The experimental results indicated that the MFL-MAARN model effectively reproduced the true defect morphology for rectangular, cylindrical, conical, regular, and irregular defects, accurately capturing defect depth information. The model also demonstrated high fitting accuracy for defect reconstruction from actual pipeline MFL internal inspection signals, further validating its generalization ability and robustness. This model provides efficient and accurate technical support for pipeline safety inspection.

1. Introduction

Oil and gas pipelines are crucial for national energy transportation, with over 50% in operation for more than 20 years (Wang et al., 2022). These pipelines are affected by various issues throughout their lifespan, including external interference, corrosion, pipe quality, and construction technology, making them susceptible to incidents that compromise safety, such as oil and gas leakage (Chen, 2025; Xu et al., 2024). Internal magnetic leakage detection technology has become increasingly prevalent in the industrial sector due to its reliability in identifying and quantifying pipeline defects (Chen et al., 2024, 2026; Dai et al., 2026). A comprehensive data and safety analysis of the detection results enables the evaluation of the remaining load-bearing capacity and service life of a pipeline, providing a scientific basis for subsequent maintenance decisions. The continuous expansion of the pipeline transportation industry has rapidly increased the number of detection tasks, resulting in a notable surge in data processing demands (Wang et al., 2021). Extensive research on the intelligent recognition and quantitative analysis of magnetic leakage detection signals will help enhance the accuracy and efficiency of detection technology, promoting pipeline monitoring toward a more intelligent approach (Wang et al., 2024; Liu et al., 2023a,b). This is crucial for ensuring the safe operation of oil and gas pipelines and reducing the risk of accidents.

* Corresponding author.
E-mail address: shdong@cup.edu.cn (S.-H. Dong).
Peer review under the responsibility of China University of Petroleum (Beijing).

https://doi.org/10.1016/j.petsci.2026.03.039

In practical pipeline integrity management, three-dimensional defect contour inversion serves as a critical intermediate step between signal acquisition and structural integrity assessment. Accurate reconstruction of defect geometry-including length, width, depth distribution, and edge morphology-provides essential input parameters for remaining strength evaluation models such as ASME B31G, Modified B31G, DNV RP-F101, and API 579 fitness-for-service procedures. Industrial guidelines (e.g., SY/T 6597-2018; API 1163-2013) generally recommend that qualified in-line inspection systems control depth quantification errors within approximately $\pm$10% of wall thickness. This tolerance range offers a practical reference for evaluating the quantitative performance of defect inversion methods. Defect depth quantification and three-dimensional (3-D) contour reconstruction are primary factors in assessing pipeline integrity during magnetic flux leakage (MFL) detection signal analysis (Wang et al., 2025; Liu et al., 2023a,b; Li et al., 2025; He et al., 2025). Their primary purpose is to accurately determine the severity of pipeline defects and quantify their associated risk levels, providing a basis for developing risk-based maintenance plans and effective detection strategies. Current research mainly focuses on signal processing and physical model reconstruction (Zhang et al., 2023). Defects are qualitatively and quantitatively analyzed using methods such as finite element analysis and magnetic field simulation (Zhang et al., 2023; Lam et al., 2024). However, these approaches exhibit high computational complexity and poor practical performance. Current studies integrate statistical methods with signal processing algorithms, utilizing wavelet transforms, Fourier transforms, and other technologies for feature extraction (Ahmad et al., 2009; Shin et al., 2016; Yang et al., 2019). These features are then combined with machine learning algorithms such as support vector machines and decision trees to quantify the defects and reconstruct their 3-D contours. However, these methods still exhibit deficiencies in feature selection and model generalization capabilities, making it difficult to accurately reconstruct the shape, size, and depth information of defects. These techniques are highly susceptible to noise interference and detection conditions, resulting in low defect quantification accuracy during pipeline MFL detection.

In existing pipeline inspection studies, deep learning techniques have been widely applied to defect detection, classification, and size estimation. However, research specifically targeting three-dimensional (3-D) defect shape inversion based on tri-axial magnetic flux leakage (MFL) signals remains limited. Existing methods can generally be categorized into three groups: physics- or traditional learning-driven inversion approaches, multi-directional or system-level enhancement methods, and data-driven approaches primarily designed for defect detection or diagnosis. Early studies combined physics-based features with conventional machine learning models to achieve defect profile reconstruction. Piao et al. (2019) employed key physical parameters and support vector machines for fast 3-D defect reconstruction, though with limited capability in representing complex defect morphologies. To improve inversion observability, Li et al. (2024) introduced multi-directional MFL excitation and sensing to reconstruct defect opening profiles, at the expense of increased system complexity. More recently, deep learning has been introduced for quantitative MFL analysis, but most studies focus on defect detection or size assessment rather than full 3-D shape inversion, such as YOLO-based detection-regression frameworks (Xie et al., 2025; Chen et al., 2024, 2026).

Beyond MFL-based inversion, fusion-based and intelligent inspection methods have also been developed in the broader pipeline inspection field, including physically coupled electromagnetic acoustic and magnetic sensing systems (Tang et al., 2025), reinforcement learning-based eddy current diagnostic frameworks (Su et al., 2024), and multi-layer feature boosting strategies for intelligent pig systems (Xu et al., 2023). The aforementioned detection methods that integrate physical models with artificial intelligence represent a significant advancement in this field, having made landmark contributions to achieving precise defect identification and intelligent diagnosis. Nevertheless, a core challenge remains: these pioneering explorations have yet to effectively address the difficulties in unifying the processing of multi-axis heterogeneous signals and clearly delineating defect geometric boundaries in MFL-based 3-D inversion tasks. To address the limitations of insufficient multi-axis feature fusion and edge blurring in depth reconstruction, this paper proposes a 3-D pipeline defect contour inversion model that integrates direction-aware multi-axis MFL signal fusion with depth–gradient joint decoding. Multi-branch convolution combined with a spatial attention mechanism is employed to independently extract and adaptively fuse tri-axial MFL features, while a dual-task decoder jointly predicts defect depth and its gradient to enhance reconstruction accuracy and boundary preservation. The proposed method provides an effective solution for high-precision defect contour reconstruction in practical pipeline inspection scenarios and offers new insights for improving the safety and reliability of oil and gas pipeline integrity assessment.

Defect depth accuracy is a dominant factor influencing burst pressure prediction and residual strength estimation. High-precision 3-D contour inversion is not only beneficial for visual reconstruction but also plays a decisive role in quantitative safety assessment and maintenance decision-making. Tri-axial MFL measurements provide complementary information about defect geometry. The axial, circumferential, and radial magnetic field components exhibit different sensitivities to defect length, width, depth, and edge morphology, jointly constraining the defect shape in the signal feature space. Previous studies have shown that although local non-uniqueness may exist in MFL inversion, multi-channel magnetic measurements enable statistically distinguishable representations for different defect morphologies and size combinations under realistic inspection conditions (Lan et al., 2019). This physical and statistical basis supports the feasibility of data-driven approaches to approximate a stable inverse mapping when trained on sufficiently diverse and representative datasets. In this work, the proposed model further exploits this property by integrating direction-aware tri-axial signal fusion, spatial coordinate encoding, and depth-gradient joint learning to enhance feature separability and inversion stability. Such a design aims to improve the robustness and reliability of 3-D defect contour reconstruction in practical pipeline inspection scenarios.

2. Model and method

2.1. Model architecture

This paper proposes a 3-D pipeline defect contour inversion framework based on the MFL-MAARN model, as illustrated in Fig. 1. To address the heterogeneous characteristics of tri-axial MFL signals, a direction-aware multi-axis dynamic fusion module is introduced, in which independent branches extract axial features and spatial attention is employed to adaptively weight the contribution of each axis.

To mitigate the blurred-edge issue commonly observed in depth-only reconstruction, a depth-gradient joint decoder is

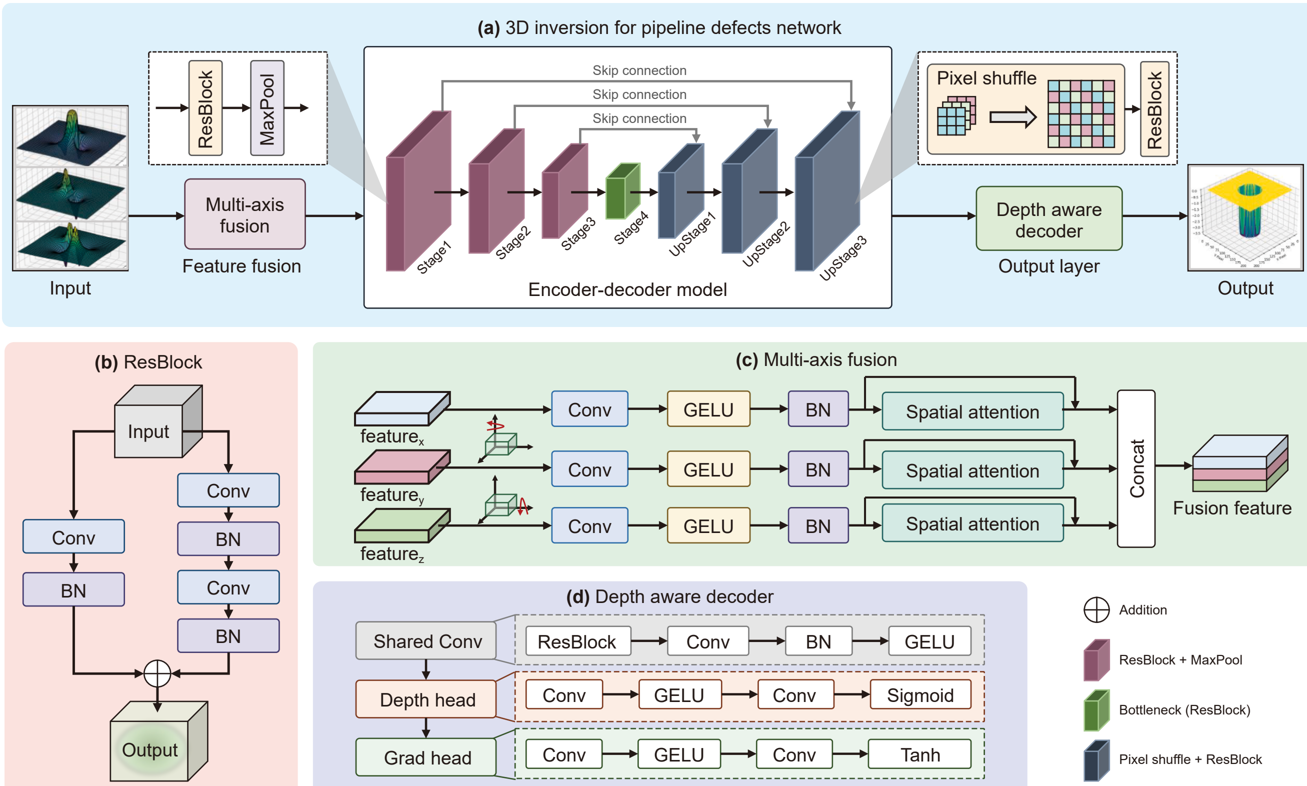

Fig. 1. Architecture of the MFL-MAARN model.

designed, where a gradient prediction branch assists depth recovery by explicitly constraining local structural variations. In addition, spatial coordinate encoding is incorporated as an input prior to enhance the network's awareness of spatial non-uniformity along the scanning path. The overall framework jointly optimizes depth accuracy and boundary consistency for 3-D defect contour inversion.

2.1.1. *Model data input and spatial coordinate encoding network*

The tri-axial MFL input signal is expressed as:

$$\mathbf{X} = [H_x,\ H_y,\ H_z] \in \mathrm{R}^{3\times H\times W} \tag{1}$$

where H_x, H_y, H_z represent the magnetic field strength of the pipe surface in the *x*, *y*, and *z* directions, respectively, while H and W denote the width and height of the image space. The 2-D coordinate encoding is as follows:

$$\mathbf{G} = \left[g_x, g_y\right] \in \mathrm{R}^{2\times H\times W} \tag{2}$$

Using 2-D normalized coordinate grid encoding, the coordinate elements are expressed as:

$$\begin{cases} g_x(i,j) = \dfrac{2j}{W-1} - 1 \\ g_y(i,j) = \dfrac{2i}{H-1} - 1 \end{cases} \tag{3}$$

For all spatial pixel positions (i,j), the spliced input signal is expressed as:

$$I = \mathrm{Concat}(\mathbf{X}, \mathbf{G}) \in \mathrm{R}^{5\times H\times W} \tag{4}$$

To explicitly incorporate spatial priors, normalized two-dimensional coordinate grids are concatenated with the MFL signals as additional channels. This coordinate encoding enables the network to directly perceive absolute spatial positions, facilitating the learning of spatially non-uniform defect characteristics induced by the scanning trajectory and improving the coupling between local magnetic responses and defect geometry.

2.1.2. *Design of direction perception multi-axis dynamic fusion module*

Considering the distinct physical responses of tri-axial MFL signals, independent convolutional branches are adopted to extract axis-specific features. A spatial attention–based dynamic fusion mechanism is then applied to adaptively weight the contribution of each axis at different spatial locations.

The tri-axial signals are input separately and defined as follows:

$$x_k \in \mathrm{R}^{1\times H\times W}, k \in \{x, y, z\} \tag{5}$$

The axial feature extraction function is expressed as:

$$f_k = F_k(x_k), f_k \in \mathrm{R}^{C'\times H\times W} \tag{6}$$

where F_k is the feature extraction subnetwork consisting of convolutional layers, batch normalization, and spatial attention. C' represents the number of channel assignments. The tri-axial splicing feature is expressed as:

$$F = \left[f_x; f_y; f_z\right] \in \mathrm{R}^{3C \times H \times W} \tag{7}$$

The generated dynamic weight is expressed as:

$$M = Softmax(M(F)), M \in \mathrm{R}^{3 \times H \times W} \tag{8}$$

where M represents the weight prediction network, including convolutional layers and activation functions.

The dynamic weighted fusion output is expressed as:

$$F_{\text{fused}}(h, \mathrm{w}) = \sum_{k=1}^{3} w_k(h, w) \cdot f_k(h, w) \tag{9}$$

$f_k(h, w) \in \mathrm{R}^{C}$ is the axial eigenvector $w_k(h, w)$ of the spatial position and (h, w) is the corresponding fusion weight.

2.1.3. Residual attention encoder design

Standard 2-D residual blocks (ResBlock2D) were introduced to enhance deep network trainability and alleviate gradient vanishing/degradation. Each block consists of two 3 × 3 convolutional layers, BatchNorm, and ReLU activation, with shortcut branches ensuring matching residual connection shapes when channel numbers change. The residual block output is:

$$\begin{cases} y_1 = \mathrm{ReLU}(\mathrm{BN}(\mathrm{Conv}_{3\times3}(x))) \\ y_2 = \mathrm{BN}(\mathrm{Conv}_{3\times3}(y_1)) \end{cases} \tag{10}$$

Each 3×3 convolutional layer used a stride of 1, padding of 1, and no bias parameters. The BatchNorm layer independently normalized the activation values of each channel, which accelerated convergence and suppressed internal covariate shifts.

The main branch output y_2 and the shortcut branch output $s(x)$ are added, followed by ReLU activation:

$$\mathrm{ResBlock2D}(x) = \mathrm{ReLU}(y_2 + s(x)) \tag{11}$$

2.1.4. Depth-gradient joint decoder design

A joint decoder was designed to predict depth and gradient maps based on shared convolutional features (Fig. 1(c)). The gradient branch enhances defect edges by focusing on local change rates, constrains boundary recovery during training, and balances training efficiency and prediction accuracy via multitask feature sharing.

The shared convolutional features are as follows:

$$F_{\text{shared}} \in \mathrm{R}^{C_\star \times H \times W} \tag{12}$$

The depth branch predicts the depth map as follows:

$$\widehat{D} = \sigma(C_{\mathrm{d}}(F_{\text{shared}})), \widehat{D} \in [0, 1]^{H \times W} \tag{13}$$

The gradient branch prediction graph is represented as follows:

$$\widehat{G} = \tanh\left(C_{\mathrm{g}}(F_{\text{shared}})\right), \widehat{G} \in [-1, 1]^{2 \times H \times W} \tag{14}$$

Among them, σ is Sigmoid activation, which ensures that the predicted depth value range is reasonable; tanh is used to output the gradient range.

2.1.5. Depth-gradient joint loss function design

To jointly supervise global depth accuracy and local boundary preservation, a depth–gradient joint loss function is employed. The overall loss is defined as a weighted combination of depth loss and gradient loss:

$$L = \alpha(\tau) \cdot L_{\mathrm{d}} + (1 - \alpha(\tau)) \cdot L_{\mathrm{g}} \tag{15}$$

where $\alpha(\tau) \in [0, 1]$ is a dynamically adjusted weighting factor with respect to the training epoch τ, which emphasizes depth accuracy in the early training stage and gradually increases the contribution of gradient supervision to enhance boundary details.

The depth loss L_{d} is defined as the L_1 distance between the predicted and ground-truth depth maps:

$$L_{\mathrm{d}} = \frac{1}{N} \sum_{i=1}^{N} |D_i - \widehat{D}_i| \tag{16}$$

where D_i and $\widehat{D}_i$ denote the ground-truth and predicted depth values at pixel i respectively, and N is the total number of pixels.

The gradient loss L_{g} is formulated using Sobel operators to constrain edge consistency:

$$L_{\mathrm{g}} = \frac{1}{N} \sum_{i=1}^{N} \left(|S_x(D_i) - S_x(\widehat{D}_i)| + \left|S_y(D_i) - S_y(\widehat{D}_i)\right|\right) \tag{17}$$

where S_x and S_y denote the horizontal and vertical Sobel gradient operators, respectively.

By jointly optimizing depth and gradient information, the proposed loss function effectively alleviates edge blurring in depth-only reconstruction and promotes structurally consistent 3-D defect contour inversion.

2.2. Model evaluation metrics

This paper adopted the image quality evaluation method in the graphics field and defined indicators such as root mean square error (E_{m}), mean positive error (E_{p}), mean negative error (E_{n}), and structural similarity index metric (SSIM), to evaluate the defect contour inversion results (Long et al., 2021; Wang et al., 2004).

The measurement points were uniformly distributed in the defect area in the axial and circumferential directions. For the contour matrix size $m \times n$, the predicted defect contour (**DP**) is:

$$\mathbf{DP} = \begin{bmatrix} DP_{11} & DP_{12} & \cdots & DP_{1n} \\ DP_{21} & DP_{22} & \cdots & DP_{2n} \\ \cdots & \cdots & \cdots & \cdots \\ DP_{m1} & DP_{m2} & \cdots & DP_{mn} \end{bmatrix}_{m \times n} \tag{18}$$

The true defect profile (**DR**) is:

$$\mathbf{DR} = \begin{bmatrix} DR_{11} & DR_{12} & \cdots & DR_{1n} \\ DR_{21} & DR_{22} & \cdots & DR_{2n} \\ \cdots & \cdots & \cdots & \cdots \\ DR_{m1} & DR_{m2} & \cdots & DR_{mn} \end{bmatrix}_{m \times n} \tag{19}$$

The E_m reflects the overall deviation between the predicted defect inversion profile and the true defect profile, as follows:

$$E_m = \sqrt{\frac{\sum_{i=1}^{m} \sum_{j=1}^{n} \left(DP_{ij} - DR_{ij}\right)^2}{\sum_{i=1}^{m} \sum_{j=1}^{n} DR_{ij}^2}} \tag{20}$$

where DP_{ij} and DR_{ij} are the respective ratios of the remaining wall thickness of the pipe to the original wall thickness of the pipe at the ith axial and the jth circumferential measurement points of the inverted defect profile and the true defect profile.

The average positive error E_p reflects the average percentage by which the predicted defect profile exceeds the true defect profile depth, that is:

$$E_p = \frac{1}{N_{pos}} \sum_{i=1}^{m} \sum_{j=1}^{n} \varepsilon_{(DP_{ij}-DR_{ij})} \left(DP_{ij} - DR_{ij}\right) \tag{21}$$

where ε is the unit step function and N_{pos} is DP_{ij} the number of measurement points greater than DR_{ij}.

The average negative error E_n reflects the average percentage of the predicted defect contour depth that is less than the actual defect contour, that is:

$$E_n = \frac{1}{N_{neg}} \sum_{i=1}^{m} \sum_{j=1}^{n} \varepsilon_{(DR_{ij}-DP_{ij})} \left(DR_{ij} - DP_{ij}\right) \tag{22}$$

where N_{neg} is DP_{ij}, the number of measurement points less than DR_{ij}.

The inverted 3-D contour and the true defect contour were regarded as two grayscale images. The SSIM was introduced to evaluate the similarity between the images, as well as between the inverted 3-D and true defect contours. The calculation formula is as follows:

$$\mathrm{SSIM}(x,y) = \frac{\left(2\mu_x\mu_y + c_1\right)\left(2\sigma_{xy} + c_2\right)}{\left(\mu_x^2 + \mu_y^2 + c_1\right)\left(\sigma_x^2 + \sigma_y^2 + c_2\right)} \tag{23}$$

where μ_x and μ_y are the mean values of x and y, respectively. σ_x^2 and σ_y^2 represent the variances of x and y, respectively. σ_{xy} is the covariance of μ_x and μ_y. $c_1 = (k_1L)^2$, $c_2 = (k_2L)^2$ is a constant used to maintain stability. L is the dynamic pixel range, while k_1 and k_2 are constants of 0.01 and 0.03 constants, respectively.

A smaller E_m indicates that the inverted contour is closer to the true contour. The relative size of E_p and E_m reflects whether the error distribution between the inverted contour and the true contour is uniform. The SSIM result ranges from 0 to 1. The closer the inverted contour image is to the true contour, the closer the SSIM is to 1. When the inverted contour is identical to the true contour, SSIM = 1.

3. Experimental setup and datasets

3.1. Database establishment

The database sources included simulation and experimental datasets. This study has constructed a three-dimensional simulation database, based on the magnetic dipole model. The constructed simulation database intentionally covers a wide range of defect morphologies (Chen et al., 2026; Xu et al., 2025), including axisymmetric, elliptical, rectangular, circular, and irregular defects, with randomly sampled size combinations. This design aims to enhance the statistical separability of different defect types in the tri-axial MFL feature space and to ensure robustness and generalization of inversion models. The simulation, which yielded 34,880 sets of MFL signals corresponding to defects (Carvalho et al., 2006).

A total of 120 sets of tri-axial MFL signals associated with machined standard defects were obtained through controlled pull-through experiments. These defects were fabricated in accordance with NB/T 47013.12-2015 Appendix B and represent standardized geometries commonly used for inspection system calibration and performance evaluation. The combined dataset (35,000 samples) was divided into training, validation, and testing subsets with a ratio of 7:2:1. The experimental pull-through data were primarily used for independent testing and performance evaluation.

3.1.1. 3-D simulation defect data

The defect morphologies in real pipeline environments are diverse. This paper generated a 3-D defect database using a 3-D gridded magnetic dipole model for MFL calculation (Liu et al., 2022; Lu et al., 2018). This method simulated the complex geometric features of real pipeline defects, providing theoretical data support for detection algorithm training. The principles of 3-D gridding discretization and magnetic dipole superposition were applied to effectively quantify the defect size, orientation, and MFL. The magnetic field intensity $P(x,y,z)$ generated at any point in space is expressed as follows:

$$\begin{aligned} H_x = \frac{\sigma_s}{4\pi}\Bigg(& \arctan\frac{(y+l)(z+d)}{(x+a)\sqrt{(x+a)^2+(y+l)^2+(z+d)^2}} - \arctan\frac{(y+l)z}{(x+a)\sqrt{(x+a)^2+(y+l)^2+z^2}} \\ & -\arctan\frac{(y-l)(z+d)}{(x+a)\sqrt{(x+a)^2+(y-l)^2+(z+d)^2}} + \arctan\frac{(y-l)z}{(x+a)\sqrt{(x+a)^2+(y-l)^2+z^2}} \\ & -\arctan\frac{(y+l)(z+d)}{(x-a)\sqrt{(x-a)^2+(y+l)^2+(z+d)^2}} + \arctan\frac{(y+l)z}{(x-a)\sqrt{(x-a)^2+(y+l)^2+z^2}} \\ & +\arctan\frac{(y-l)(z+d)}{(x-a)\sqrt{(x-a)^2+(y-l)^2+(z+d)^2}} - \arctan\frac{(y-l)z}{(x-a)\sqrt{(x-a)^2+(y-l)^2+z^2}}\Bigg) \end{aligned} \tag{24}$$

$$H_y = \frac{\sigma_s}{4\pi}\left(\ln\frac{\left\{z+d+\sqrt{(x+a)^2+(y-l)^2+(z+d)^2}\right\}\left\{z+\sqrt{(x+a)^2+(y+l)^2+z^2}\right\}}{\left\{z+\sqrt{(x+a)^2+(y-l)^2+z^2}\right\}\left\{z+d+\sqrt{(x+a)^2+(y+l)^2+(z+d)^2}\right\}} - \ln\frac{\left\{z+d+\sqrt{(x-a)^2+(y-l)^2+(z+d)^2}\right\}\left\{z+\sqrt{(x-a)^2+(y+l)^2+z^2}\right\}}{\left\{z+\sqrt{(x-a)^2+(y-l)^2+z^2}\right\}\left\{z+d+\sqrt{(x-a)^2+(y+l)^2+(z+d)^2}\right\}}\right) \quad (25)$$

$$H_z = \frac{\sigma_s}{4\pi}\left(\ln\frac{\left\{y+l+\left[(x+a)^2+(y+l)^2+z^2\right]\right\}\left\{y-l+\left[(x+a)^2+(y-l)^2+(z+d)^2\right]\right\}}{\left\{y-l+\left[(x+a)^2+(y-l)^2+z^2\right]\right\}\left\{y+l+\left[(x+a)^2+(y+l)^2+(z+d)^2\right]\right\}} - \ln\frac{\left\{y+l+\left[(x-a)^2+(y+l)^2+z^2\right]\right\}\left\{y-l+\left[(x-a)^2+(y-l)^2+(z+d)^2\right]\right\}}{\left\{y-l+\left[(x-a)^2+(y-l)^2+z^2\right]\right\}\left\{y+l+\left[(x-a)^2+(y+l)^2+(z+d)^2\right]\right\}}\right) \quad (26)$$

where l and a are the half-length and half-width of the rectangular defect, respectively, d is the rectangular defect depth, and σ_s is the surface magnetic charge density.

The gridded magnetic dipole model used a grid M to decompose an irregular defect into several small defects with regular shapes. The leakage magnetic field response of each small defect was superimposed $H_{M_{i,j}}$ to obtain the composite field of the irregular defect. The magnetic field contribution of all the small grid units was accumulated to generate the overall leakage magnetic field distribution map $M_{i,j}$. The composite field of the grid is expressed as follows:

$$H(x,y,z) = \sum_{i=1}^{n}\sum_{j=1}^{m} H_{M_{i,j}}(x,y,z) \quad (27)$$

where n and m represent the length and width of the grid, respectively, and $H(x,y,z)$ denotes the composite field of irregular defects. A finer grid yielded a higher signal simulation accuracy.

The grid center $(0,0)$ was used as the center point during defect generation. The defect length L (ranging from 0 mm to 40 mm), width W (ranging between 0 mm and 40 mm), and depth D (10% to 70% of the pipe wall thickness) were randomly selected. A defect grid M with a maximum depth of D was constructed within the specified length L and width W parameters. The generated defect types included axisymmetric, elliptical, rectangular, circular, and 3-D irregular defects, totaling 34,880 randomly generated defect groups.

3.1.2. Experimental pulling defect data

A pull-through MFL inspection experiment was conducted using a fifth-generation ultra-high-definition internal MFL detector developed by China University of Petroleum (Beijing) as shown in Fig. 2. The test was performed on a ϕ 323 mm × 7 mm pipeline segment and the inspection tool was pulled through the pipeline at a controlled constant speed of 1 m/s. A total of 120 machined defect specimens were fabricated in accordance with NB/T 47013.12-2015 Appendix B, and seven representative defect categories, including general metal loss, pitting, and axial groove-type metal loss, were designed to cover practical inspection geometries.

3.2. Model parameter setting

The model was trained using an AdamW optimizer, which was combined with weight decay to prevent overfitting. The OneCycleLR learning rate scheduling strategy was introduced to further improve training stability. An early stopping mechanism was implemented to prevent the model from falling into local optimality, which terminated training early when the validation loss did not significantly decrease within 10 consecutive epochs. During the testing phase, morphological operations were employed to refine the defect depth image generated by the model, aiming to

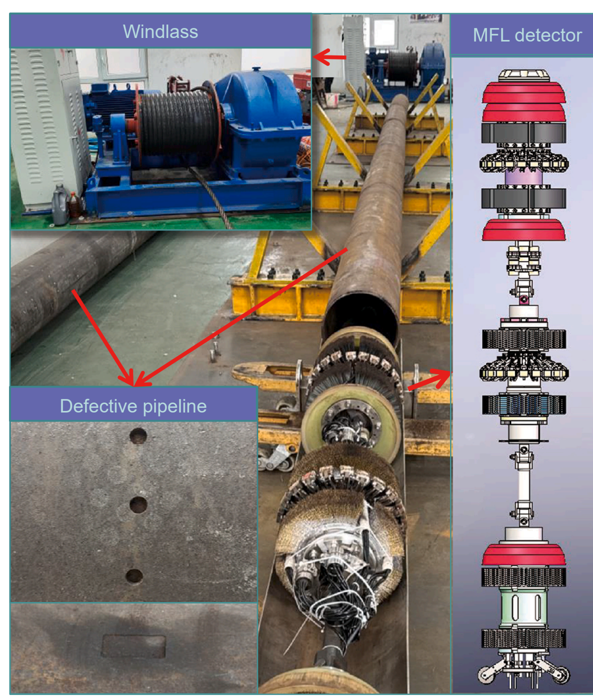

Fig. 2. Pulling test bench.

remove noise and minor artifacts. Both 2-D and 3-D visualization methods were used to illustrate the defect outlines.

During preprocessing, the data was normalized to ensure that all channel information was distributed within a reasonable range. Channel-wise min-max normalization was applied using the global minimum and maximum values computed from the training dataset. As a linear monotonic transformation, this scaling preserves the relative spatial distribution and amplitude

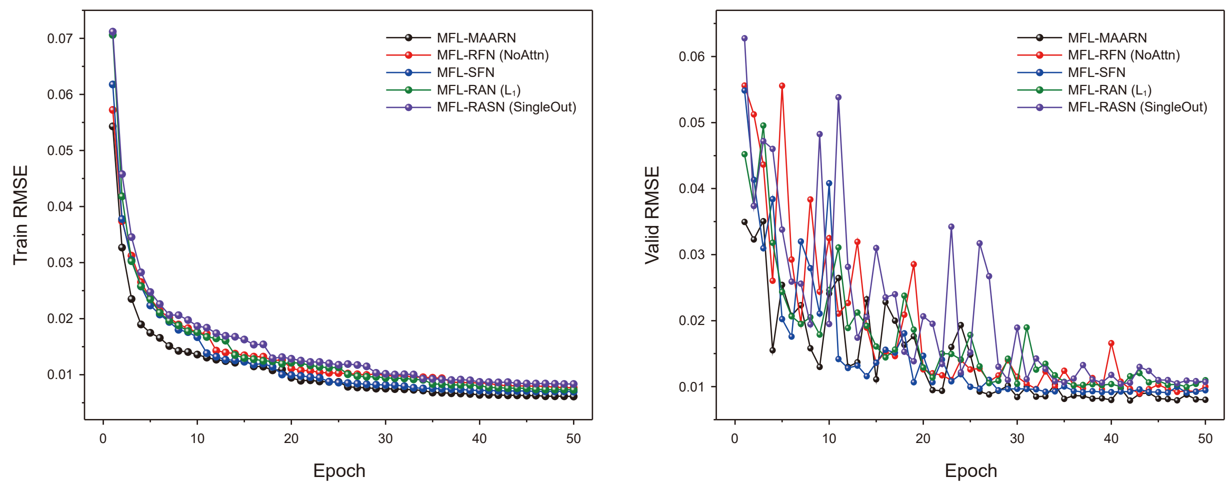

(a) RMSE during the training and verification process

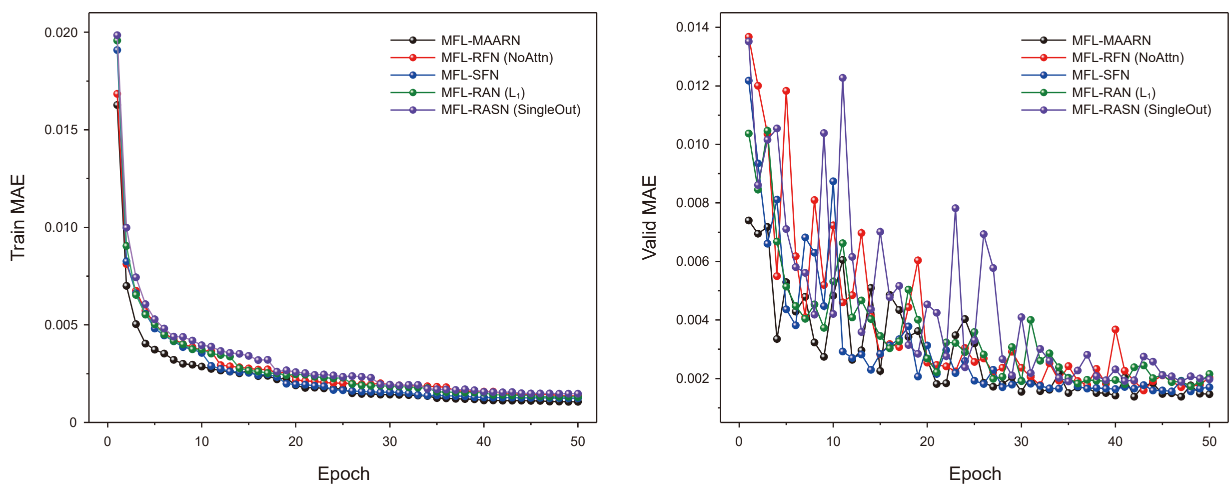

(b) MAE during the training and verification process

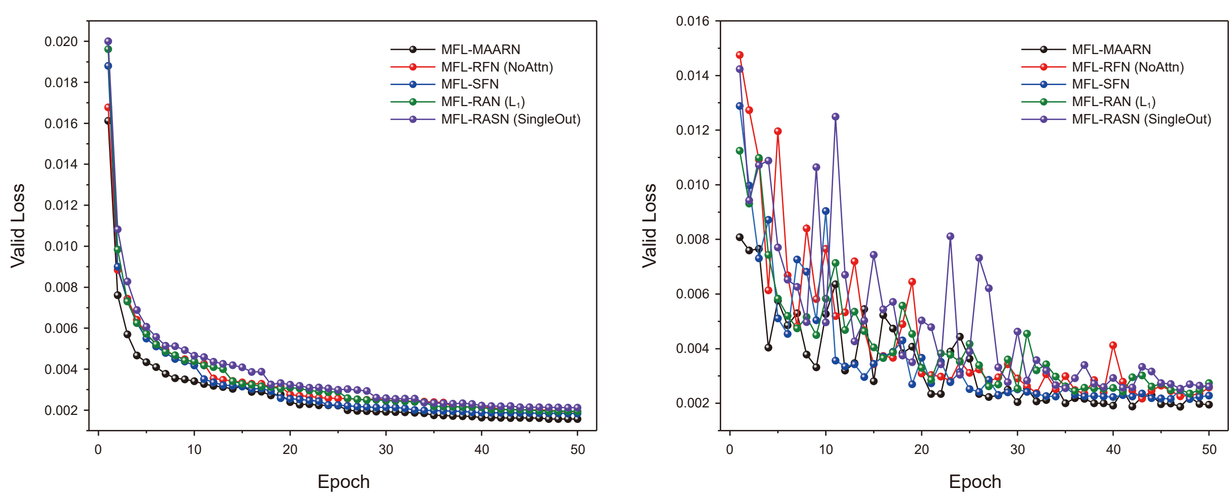

(c) Loss during the training and verification process

Fig. 3. A comparison of the training process of the ablation experiment (training set on the left and validation set on the right).

Table 1
Statistics of the model test results.

Model	E_m	E_p	E_n	SSIM
MFL-MAARN	0.0842	0.0487	0.0086	0.9955
MFL-RFN (NoAttn)	0.0940	0.0616	0.0088	0.9759
MFL-SFN	0.0972	0.0617	0.0091	0.9392
MFL-RAN (L_1)	0.1067	0.0830	0.0088	0.9217
MFL-RASN (SingleOut)	0.1078	0.0689	0.0106	0.9050

relationships of the MFL signals while improving numerical stability during network optimization. Data augmentation, such as random flipping and rotation, was also used to expand the training samples and improve model accuracy. Data loading was performed in a multithreaded manner, utilizing the PyTorch DataLoader for batch reading and dynamic shuffling to ensure balanced data distribution during training. The batch size was set to 24, and the number of epochs was set to 50.

3.3. Ablation experiment

Four sets of ablation experiments were designed and compared with the complete model to quantitatively evaluate the impact of multi-axis branches, spatial attention, residual structures, dual-branch output, and joint loss.

(1) MFL-RFN (NoAttn): The full MFL-RARN model was used to remove all spatial attention and multi-axis dynamic weighting components, leaving only the per-axis convolution + ResBlock splicing fusion. This variant reflected the contribution of the attention mechanism to the feature extraction and fusion of the multi-axis MFL signals.
(2) MFL-SFN: The three-channel MFL signals were directly spliced into a single convolution + ResBlock network without independent multi-axis branching. This variant can be used to evaluate the difference between axis-by-axis branching and simple splicing fusion in terms of feature expression and final reconstruction performance.
(3) MFL-RAN (L_1): Although the complete network structure was retained, only the L_1 loss of deep reconstruction was used during training, removing the explicit gradient loss term. The benefit of using both the gradient loss and simple L_1 was verified.
(4) MFL-RASN (SingleOut): Although the multi-axis branch, spatial attention module, and residual structure were retained, only the depth branch was produced, and the gradient branch was removed. The loss function only calculated the L_1 of the depth reconstruction, along with an optional numerical gradient regularization to verify the significance of the explicit gradient branch (Gradient Head) in assisting depth reconstruction.

4. Results and discussion

4.1. Comparison between the model training and test indicators

Fig. 3 presents the training dynamics of the proposed model. The training and validation loss, along with the MAE and RMSE curves, decrease rapidly during the initial stage and gradually stabilize as training proceeds. The OneCycleLR learning rate scheduling strategy facilitates effective global optimization, while an early stopping mechanism terminates training when the validation loss shows no significant improvement over 10 consecutive epochs, thereby preventing overfitting.

As shown in Fig. 3, all five models exhibit a sharp reduction in loss, RMSE, and MAE within the first 10 epochs, followed by a slower decline from epochs 11 to 50. The training and validation metrics remain closely aligned, indicating good generalization performance of the proposed MFL-MAARN model. Mild oscillations in the validation loss are observed, mainly due to the joint optimization of depth and gradient losses with dynamically adjusted weighting, as well as the nonlinear and ill-posed nature of 3-D defect inversion from MFL signals. Nevertheless, the overall

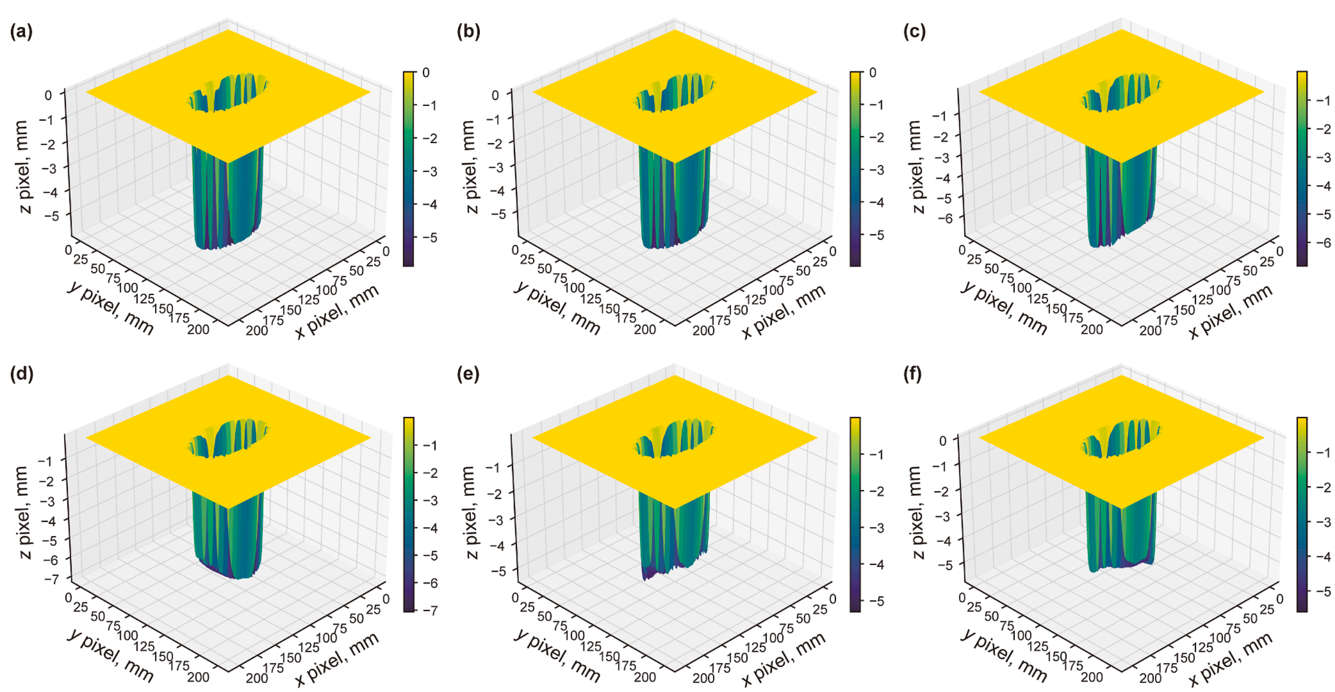

Fig. 4. The inversion results of the regular defects.

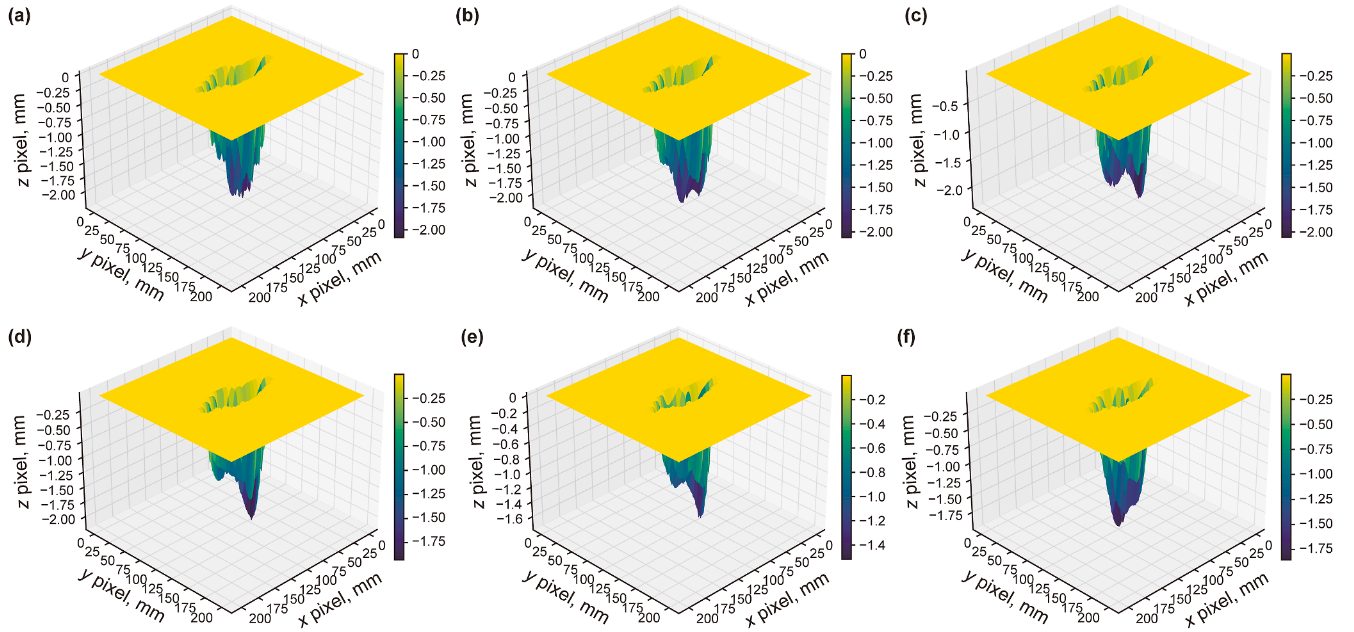

Fig. 5. The inversion results of the irregular defects.

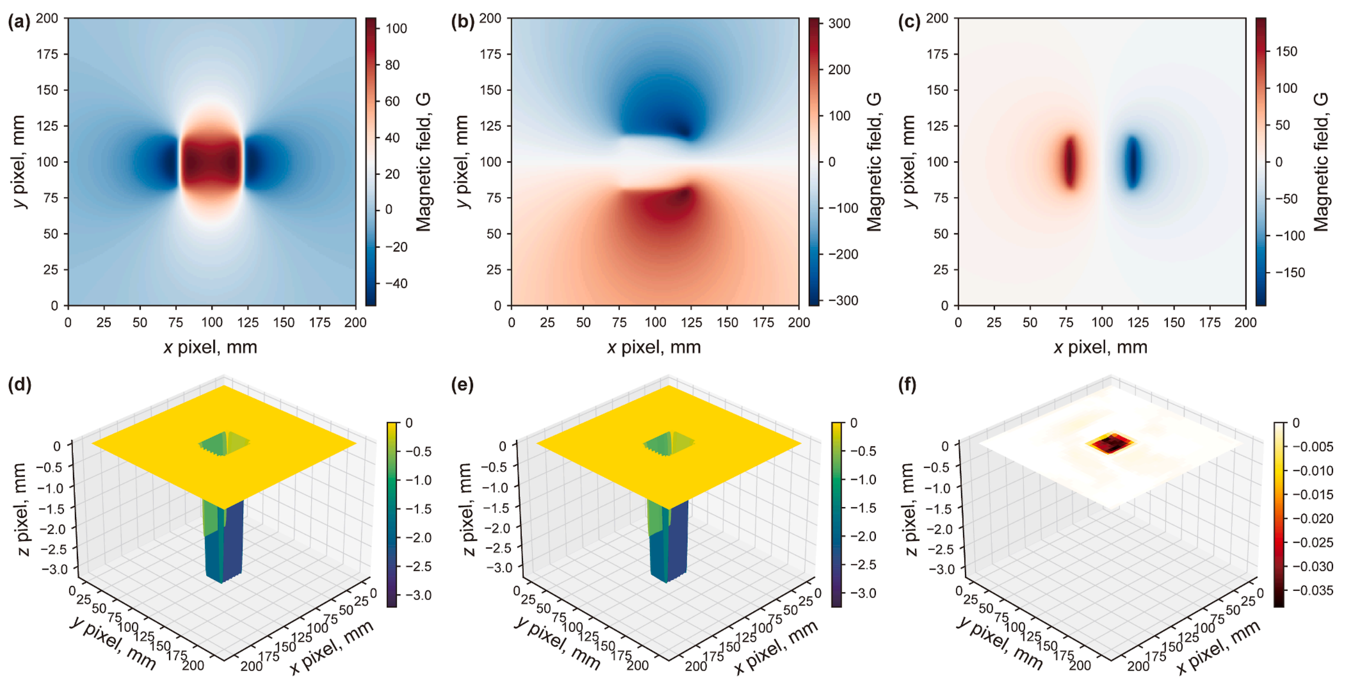

Fig. 6. The inversion results of rectangular defects. **(a)**–**(c)** *Bx*, *By*, and *Bz* data of the defect; **(d)** original 3-D image of the defect; **(e)** reconstructed 3-D image; **(f)** 3-D image of the reconstruction error, respectively. *Bx* is the magnetic flux leakage in the *x*-direction, *By* is the magnetic flux leakage in the *y*-direction, and *Bz* is the magnetic flux leakage in the *z*-direction.

validation loss converges steadily, and the final model demonstrates stable performance on the test set.

The trained model was assessed using the test set. As shown in Table 1, the MFL-MAARN model yielded optimal E_{m}, E_{p}, E_{n}, and SSIM values of 0.0842, 0.0487, 0.0086, and 0.9955, respectively. These results confirmed the accuracy of the method proposed in this paper in reconstructing 3-D defect models. Comparisons indicated that our model outperformed the MFL-MAARN, MFL-RFN (NoAttn), MFL-SFN, MFL-RAN (L_1), and MFL-RASN (SingleOut) models in both detail recovery and global structure reconstruction.

4.2. Defect 3-D contour inversion and comparison

4.2.1. Regular defect inversion

Fig. 4 shows the reconstruction of the 3-D contour of a regular defect using five models. Fig. 4(a)–(f) show the original defect morphology, MFL-MAARN, MFL-RFN (NoAttn), MFL-SFN, MFL-RAN (L_1), and MFL-RASN (SingleOut) models, respectively. For regular defects, the proposed method showed higher accuracy in reconstructing defect size, opening contour, and overall shape using MFL-MAARN, followed by the MFL-SFN model. The MFL-SFN, MFL-

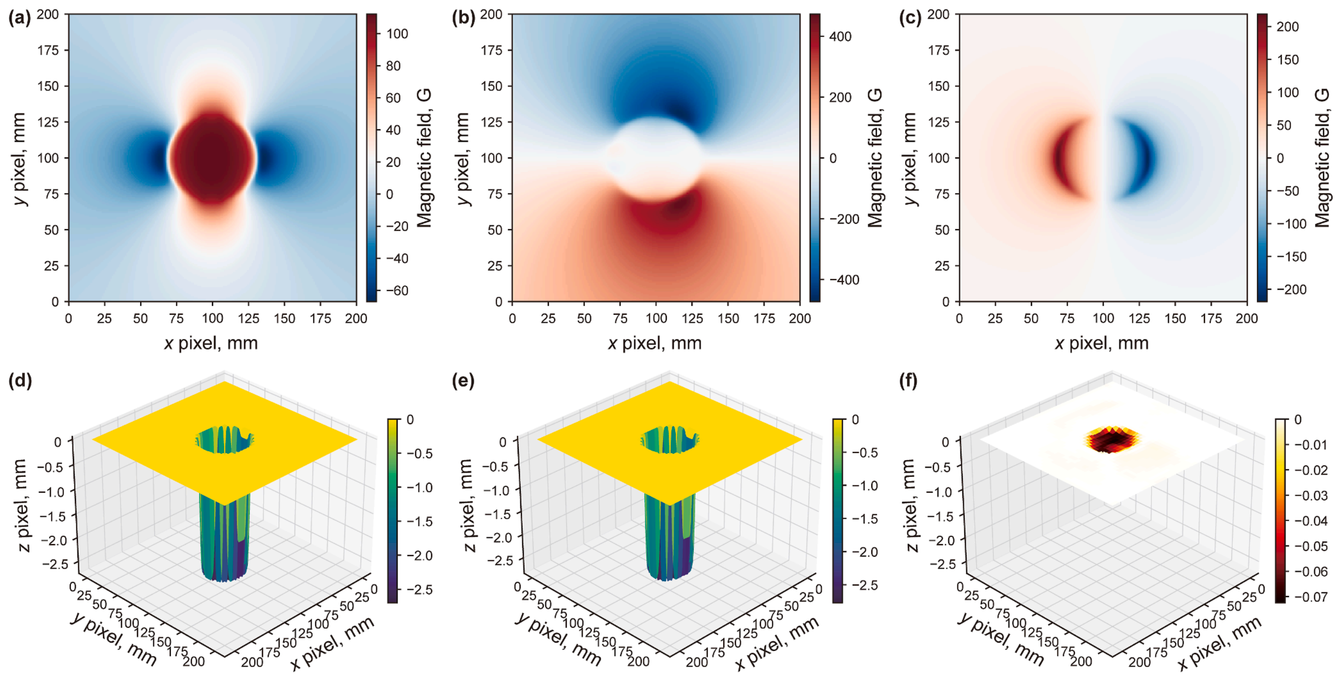

Fig. 7. The inversion results of cylindrical defects.

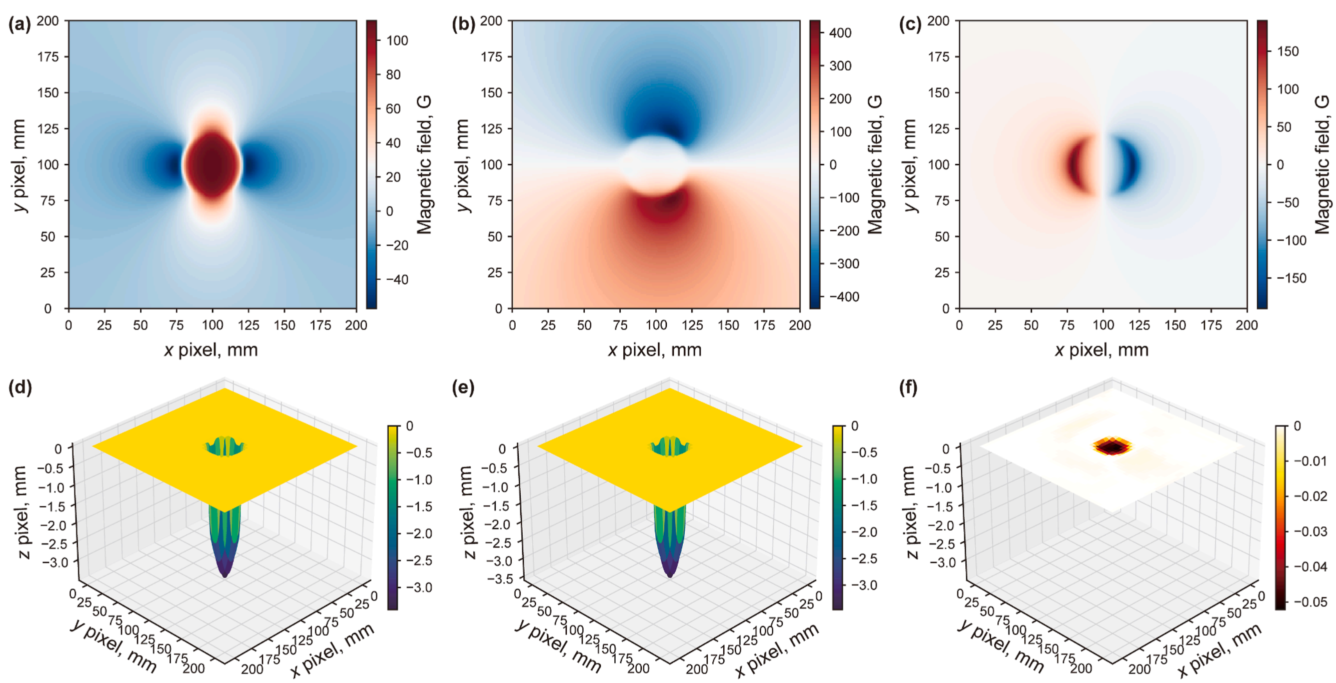

Fig. 8. The inversion results of conical defects.

RAN (L_1), and MFL-RASN (SingleOut) models performed poorly in fitting the true contour.

4.2.2. Irregular defect inversion

Fig. 5 shows the reconstruction results of an irregular defect using the five models. Fig. 5(a)–(f) show the original defect shape, MFL-MAARN, MFL-RFN (NoAttn), MFL-SFN, MFL-RAN (L_1), and MFL-RASN (SingleOut), respectively. The MFL-MAARN model performed best for irregular defects, while the MFL-SFN, MFL-SFN, MFL-RAN(L_1), and MFL-RASN (SingleOut) models exhibited poor depth fitting accuracy. Comparative analysis across multiple experimental groups revealed that the four control groups in the ablation experiments displayed defect edge blurring and lacked global structural constraints. The proposed deep attention network-based method, leveraging a residual structure and attention gate mechanism, enabled the model to capture detailed

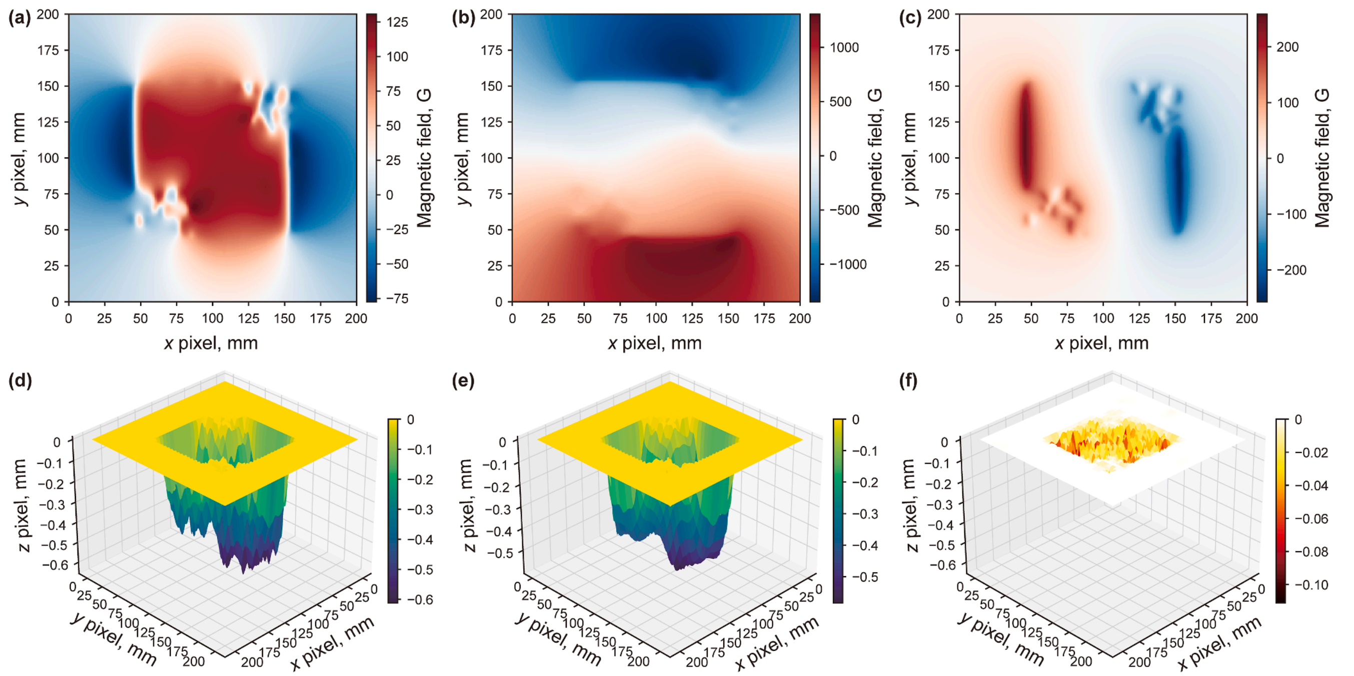

Fig. 9. The inversion results of the irregular defects.

variations while maintaining overall contour consistency. This yielded superior quantitative and visual performance results compared to the control group.

4.3. Defect 3-D contour reconstruction

4.3.1. Cuboid defects

This paper compared 2-D and 3-D images to demonstrate the difference between the predicted results and the true defect depth images and validate the efficacy of the model. Fig. 6 shows the original and reconstructed defect morphologies of rectangular defects after 3-D reconstruction.

The MFL-MAARN model yielded an average E_m of 0.0100, E_p of 0.0007, E_n of 0.0012, and SSIM of 0.9982 during the 3-D reconstruction of the rectangular defect. The 3-D image reconstructed using the MFL-MAARN model accurately reproduced the local details and overall contours of the original image. The absolute error graph exhibited low error values, indicating that the model accurately captured the defect depth information. Analysis showed that the real and predicted 2-D images displayed similar defect edges and depth changes. Post-processing significantly suppressed local noise in the error image, further verifying model accuracy.

4.3.2. Cylindrical defects

Fig. 7(a)–(f) display the magnetic flux density components and 3-D visualization results of the defect: (a)–(c) are the *Bx*, *By*, and *Bz* data, respectively; (d)–(f) depict the original 3-D image, the reconstructed 3-D image, and the 3-D image of the reconstruction error, respectively.

The MFL-MAARN model yielded an average E_m of 0.0212, E_p of 0.0022, E_n of 0.0035, and SSIM of 0.9974 during the 3-D reconstruction of the cylindrical defect. The 3-D image of the cylindrical defect reconstructed using the MFL-MAARN model accurately reproduced the defect opening shape of the original image, showing clear edge contours. The depth error between the reconstructed and the original images was less than 0.07 mm. In addition, the reconstructed contour preserves consistent axial extension and opening-shape characteristics compared with the ground truth morphology, indicating stable geometric consistency of safety-critical parameters (e.g., defect depth and length) for engineering reference.

4.3.3. Conical defects

Fig. 8(a)–(c) present the *Bx*, *By*, and *Bz* data of the defect, respectively, while Fig. 8(d)–(f) show the original 3-D image, the reconstructed 3-D image, and the 3-D image of the reconstruction error, respectively.

The MFL-MAARN model yielded an average E_m of 0.0157, E_p of 0.0005, E_n of 0.0014, and SSIM of 0.9923 during the 3-D reconstruction of the conical defect, confirming its superior performance. The 3-D image of the rectangular defect reconstructed using the MFL-MAARN model displayed a high degree of similarity to the original image in terms of the defect opening shape and depth-direction morphology.

4.3.4. Irregular defects

The *Bx*, *By*, and *Bz* data of the defect are shown in Fig. 9(a)–(c), respectively. The original 3-D image of the defect, its reconstructed counterpart, and the corresponding 3-D reconstruction error image are presented in Fig. 9(d)–(f).

The MFL-MAARN model yielded average metrics of E_m 0.1185, E_p 0.0243, E_n 0.0056, and SSIM 0.9956 during the 3-D reconstruction of the irregular defect. The 3-D image reconstructed using the MFL-MAARN model accurately reproduced the defect opening shape of the original image, showing clear edge contours. The reconstructed image in the depth direction exhibited smoother edges than the original image. This was due to the post-processing of the defect depth image produced by the model, which utilized morphological opening to eliminate noise and minor artifacts.

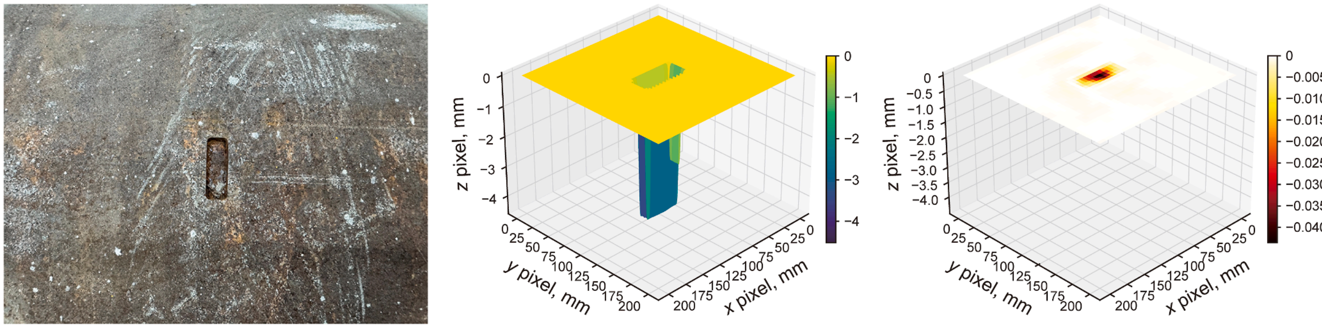

Fig. 10. The defect inversion results of the pipeline pulling test.

4.3.5. Quantitative performance analysis

A comprehensive quantitative comparison across the four representative defect types (rectangular, cylindrical, conical, and irregular) demonstrates stable dimensional reconstruction capability of the proposed MFL-MAARN model. For rectangular, cylindrical, and conical defects, the average relative error Em remains within 0.01–0.0212, with SSIM values exceeding 0.99, indicating high structural fidelity. In particular, for cylindrical defects, the maximum absolute depth error is less than 0.07 mm under a wall thickness of 7 mm, corresponding to approximately 1% of wall thickness. Even for irregular defects with more complex geometries, the reconstructed contours maintain high structural similarity (SSIM = 0.9956), demonstrating robust geometric consistency. Overall, the inversion results exhibit small depth-related deviations relative to wall thickness and stable quantitative consistency across different defect morphologies, confirming the effectiveness of the proposed framework in three-dimensional geometric reconstruction under controlled validation conditions.

5. Experimental verification

Due to the high cost, operational risk, and safety constraints associated with full-scale pipeline inspection experiments, the availability of real defect samples is inherently limited in most MFL-based studies. Consequently, machined standard defects are widely adopted in engineering practice to evaluate whether a proposed inversion model trained on simulated data can be effectively transferred to real inspection signals. In this context, the pull-through experiment shown in Fig. 10 is intended as an engineering-level validation rather than a large-scale statistical assessment.

The pull-through test was conducted on a ϕ 323 mm × 7 mm pipeline segment containing 60 machined defects. Although the number of defects is limited, these defects cover representative ranges of defect depth, size, and spatial distribution commonly encountered in practical pipeline inspections. This experimental design aims to reflect realistic inspection conditions while ensuring controllable and repeatable defect geometries. Furthermore, the pull-through experimental data serve as an independent testing subset within the overall dataset division described in Section 3.1. The model training phase primarily relies on large-scale simulated samples, and the experimental signals are used here exclusively for performance evaluation, ensuring objective assessment of generalization capability.

The quantitative reconstruction results obtained from the real inspection signals yield an E_{m} of 0.0274, an E_{p} of 0.0470, an E_{n} of 0.0394, and a SSIM of 0.9851. These results indicate that the proposed MFL-MAARN model achieves high reconstruction accuracy and strong structural similarity when applied to real pipeline MFL data, demonstrating satisfactory generalization from simulated training data to practical inspection scenarios.

Fig. 10 further presents representative defect inversion results from the pull-through experiment. In real pipeline inspections, data noise and variations in acquisition conditions inevitably affect signal quality and reconstruction performance. The proposed method explicitly accounts for these factors through dedicated data preprocessing and feature fusion strategies. Specifically, coordinate grid encoding is introduced to provide spatial prior information, while an attention-based fusion mechanism adaptively emphasizes informative local regions. As a result, the proposed model maintains stable reconstruction performance under varying noise levels and acquisition conditions. In addition, the use of early stopping and learning rate scheduling during training effectively mitigates overfitting, further enhancing the robustness and generalization capability of the model when applied to previously unseen inspection data.

6. Conclusions

(1) This paper proposed a 3-D pipeline defect contour inversion method based on the MFL-MAARN model and established four sets of ablation experiments. The results showed that the MFL-MAARN model yielded E_{m}, E_{p}, E_{n}, and SSIM values of 0.0842, 0.0487, 0.0086, and 0.9955, respectively, during training and testing, which all represented optimal indicators. Furthermore, the MFL-MAARN model accurately reconstructed the 3-D defect model and outperformed the comparison model in both detail recovery and global structure reconstruction.

(2) The MFL-MAARN model was based on a deep attention network approach, utilizing a residual structure and an attention gate mechanism. This allowed it to capture detail changes while maintaining overall contour consistency, resulting in superior results compared to the control group in terms of both quantitative indicators and visual effects. The results indicated that the MFL-MAARN model accurately reconstructed the size, opening contour, and overall shape of regular defects. It also exhibited superior fitting accuracy in the depth direction of irregular defects and higher precision in defect edge processing inversion.

(3) The MFL-MAARN model was used to construct a composite loss function that combined MAE and SSIM. During the training process, the model focused on pixel-level errors while considering structural image similarity, which substantially improved the quality of the reconstructed image. The experiments revealed that the MFL-MAARN model effectively captured the shape and depth changes of the defects. The SSIM values of the rectangular, cylindrical, conical, and irregular defects were 0.998, 0.9974, 0.9923,

and 0.9956, respectively, showing a high ability to retain details during defect contour reconstruction.

(4) The defect data of the machined tubular body were collected via a pulling test. The trained 3-D MFL-MAARN signal contour reconstruction model was employed to detect actual signals, yielding an E_m of 0.0274, an E_p of 0.0470, an E_n of 0.0394, and an SSIM of 0.9851. This indicated that the MFL-MAARN model also exhibited high fitting accuracy for reconstructing defects in actual MFL detection signals within the pipeline, further verifying the generalization ability and robustness of the model.

Future work will expand and optimize the defect database by incorporating newly observed defect morphologies from practical engineering inspections, thereby enhancing representation capability and adaptability. Further theoretical analysis will investigate the identifiability and stability of tri-axial MFL-based 3-D defect inversion. In addition, validation will be extended to diverse defect types, varying wall thicknesses, pipeline materials, inspection speeds, and challenging noise conditions. Systematic cross-specification evaluation will be conducted to comprehensively assess robustness, scalability, and generalization capability in practical in-line inspection scenarios.

CRediT authorship contribution statement

Lu-Shuai Xu: Writing – review & editing, Writing – original draft, Visualization, Validation, Supervision, Software, Methodology, Investigation, Formal analysis, Data curation, Conceptualization. **Shao-Hua Dong:** Supervision, Funding acquisition. **Feng Li:** Writing – review & editing, Writing – original draft. **Hao-Tian Wei:** Resources. **Cong Zuo:** Resources, Data curation. **Di Qian:** Resources, Data curation. **Peng Hou:** Resources.

Conflict of interest

All authors declare that no commercial or associative interest from any organization that may represent a conflict of interest in connection with the work submitted. And there are no other relationships or activities that could appear to have influenced the submitted work.

Acknowledgement

This research was supported by Strategic Cooperation Technology Projects of China National Petroleum Corporation (CNPC) and China University of Petroleum, Beijing (CUPB) (ZLZX2020-05).

References

Ahmad, K.-R., Reilly, J.-P., Nikolova, K.-N., et al., 2009. Machine learning techniques for the analysis of magnetic flux leakage images in pipeline inspection. IEEE Trans. Magn. 45 (8), 3073–3084. https://doi.org/10.1109/TMAG.2009.2020160.

Carvalho, A.-A., Rebello, J.-M.-A., Sagrilo, L.-V.-S., et al., 2006. MFL signals and artificial neural networks applied to detection and classification of pipe weld defects. NDT E Int. 39 (8), 661–667. https://doi.org/10.1016/j.ndteint.2006.04.003.

Chen, P.-C., 2025. Advancements and future outlook of safety monitoring, inspection and assessment technologies for oil and gas pipeline networks. J. Pipeline Sci. Eng. 5 (4), 100267. https://doi.org/10.1016/j.jpse.2025.100267.

Chen, Y.-N., Tian, Z.-G., Wei, H.-T., et al., 2024. Reconstruction of 3-D pipeline defect profile based on MFL signals and hybrid neural networks. Reliab. Eng. Syst. Saf. 184, 1131–1142. https://doi.org/10.1016/j.psep.2024.02.052.

Chen, X.-M., Fu, M.-K., Shao, J., et al., 2026. A cascaded pipeline defect detection and size estimation method based on the YOLOv11 and physics-informed network using the MFL data. Pet. Sci. 23 (3), 1505–1518. https://doi.org/10.1016/j.petsci.2025.08.013.

Dai, Z.-X., Wang, T.-B., Hu, X.-G., et al., 2026. A review of data-driven leakage diagnosis methods across pipeline and energy transportation system. J. Pipeline Sci. Eng., 100459. https://doi.org/10.1016/j.jpse.2026.100459.

He, T.-J., Zhong, H.-Y., Liao, K.-X., et al., 2025. Quantitative study on magnetic flux leakage internal detection signal of defects on the outer wall of bimetal composite pipes. Int. J. Pres. Ves. Pip. 214, 105438. https://doi.org/10.1016/j.ijpvp.2025.105438.

Lam, Q.-M., Duong, V.-T., Phan, H.-L., et al., 2024. Parametric design methodology for yoke-magnetization in magnetic flux leakage detection systems. Results Eng. 23, 102669. https://doi.org/10.1016/j.rineng.2024.102669.

Lan, T., Liu, J., Qin, H., et al., 2019. Time-domain global similarity method for automatic data cleaning for multi-channel measurement systems in magnetic confinement fusion devices. Comput. Phys. Commun. 234, 159–166. https://doi.org/10.1016/j.cpc.2018.07.014.

Li, S.-P., Bai, L.-B., Zhang, X., et al., 2024. A defect opening profile reconstruction method based on multidirectional magnetic flux leakage detection. Measurement 233 (30), 114701. https://doi.org/10.1016/j.measurement.2024.114701, 114701.

Li, S.-P., Bai, L.-B., Ren, C., et al., 2025. A multidirectional magnetic flux leakage detection based crack 3-D profile reconstruction method. Mech. Syst. Signal Process. 228, 112408. https://doi.org/10.1016/j.ymssp.2025.112408.

Liu, J.-H., Shen, X.-K., Wang, J.-F., et al., 2022. An intelligent defect detection approach based on cascade attention network under complex magnetic flux leakage signals. IEEE Trans. Ind. Electron. 70 (7), 7417–7427. https://doi.org/10.1109/TIE.2022.3201320.

Liu, B., Liang, Y.-S., He, L.-Y., et al., 2023a. Quantitative study on the propagation characteristics of MFL signals of outer surface defects in long-distance oil and gas pipelines. NDT E Int. 137, 102861. https://doi.org/10.1016/j.ndteint.2023.102861.

Liu, B., Wu, Z.-H., Wang, P., et al., 2023b. Quantization of magnetic flux leakage internal detection signals for composite defects of gas and oil pipelines. Energy Rep. 9, 5899–5914. https://doi.org/10.1016/j.egyr.2023.05.025.

Long, Y., Huang, S.-L., Peng, L.-S., et al., 2021. A characteristic approximation approach to defect opening profile recognition in magnetic flux leakage detection. IEEE Trans. Instrum. Meas. 70, 1–12. https://doi.org/10.1109/TIM.2021.3050185.

Lu, S.-X., Feng, J., Zhang, H.-G., et al., 2018. An estimation method of defect size from MFL image using visual transformation convolutional neural network. IEEE Trans. Ind. Inf. 15 (1), 213–224. https://doi.org/10.1109/TII.2018.2828811.

Piao, G.-Y., Guo, J.-B., Hu, T.-H., et al., 2019. Fast reconstruction of 3-D defect profile from MFL signals using key physics-based parameters and SVM. NDT E Int. 103, 26–38. https://doi.org/10.1016/j.ndteint.2019.01.004.

Shin, H.-C., Roth, H.-R., Gao, M.-C., et al., 2016. Deep convolutional neural networks for computer-aided detection: CNN architectures, dataset characteristics and transfer learning. IEEE Trans. Med. Imag. 5 (5), 1285–1298. https://doi.org/10.1109/TMI.2016.2528162.

Su, L.-S., Gao, B., Zhao, X.-Y., et al., 2024. RHiREM: Intelligent diagnostic framework for pipeline Eddy current internal inspection based on reinforcement learning with hierarchical reward exploration mechanism. NDT E Int. 144, 103073. https://doi.org/10.1016/j.ndteint.2024.103073.

Tang, Q., Gao, B., Ma, Q.-P., et al., 2025. Physical coupling fusion of electromagnetic acoustic guided wave with "near-zero" magnetic sensing system for multitype defect detection. IEEE Trans. Instrum. Meas. 74, 1–11. https://doi.org/10.1109/tim.2025.3555696.

Wang, Z., Bovik, A.-C., Sheikh, H.-R., et al., 2004. Image quality assessment: From error visibility to structural similarity. IEEE Trans. Image Process. 13 (4), 600–612. https://doi.org/10.1109/TIP.2003.819861.

Wang, Z.-Y., Zhao, X.-D., Han, Z.-H., et al., 2021. Advanced big-data/machine-learning techniques for optimization and performance enhancement of the heat pipe technology—A review and prospective study. Appl. Energy 294, 116969. https://doi.org/10.1016/j.apenergy.2021.116969.

Wang, G., Cheng, Q., Zhao, W., et al., 2022. Review on the transport capacity management of oil and gas pipeline network: Challenges and opportunities of future pipeline transport. Energy Strategy Rev. 43, 100933. https://doi.org/10.1016/j.esr.2022.100933.

Wang, L., Zhang, H.-G., Liu, J.-H., et al., 2024. Irregular defect size estimation for the magnetic flux leakage detection system via expertise-informed collaborative network. IEEE Trans. Ind. Electron. 71 (10), 13189–13200. https://doi.org/10.1109/TIE.2024.3357845.

Wang, R.-B., Chen, Y.-Z., Yu, H.-Z., et al., 2025. Defect classification and quantification method based on AC magnetic flux leakage time domain signal characteristics. NDT E Int. 149, 103250. https://doi.org/10.1016/j.ndteint.2024.103250.

Xie, J.-L., Yang, J., Fu, K., et al., 2025. Quantitative assessment of pipeline defects utilizing a dual-stage deep learning framework: integration of pretrained YOLO network and multi-input parallel convolution architectures on magnetic flux leakage data. J. Pipeline Sci. Eng. 6 (1), 100282. https://doi.org/10.1016/j.jpse.2025.100282.

Xu, H.-W., Yang, Y.-P., Gao, B., et al., 2023. Multi-layer feature boosting framework for pipeline inspection using an intelligent pig system. IEEE Trans. Ind. Inf. 19 (7), 8406–8417. https://doi.org/10.1109/TII.2022.3217754.

Xu, H., Li, Y., Zhou, T., et al., 2024. An overview of the oil and gas pipeline safety in China. Journal of Industrial Safety 1 (1), 100003. https://doi.org/10.1016/j.jinse.2024.100003.

Xu, L.-S., Dong, S.-H., Wei, H.-T., et al., 2025. Denoising of the magnetic flux leakage signal using dynamic feature fusion and a multi-scale autoencoder network. Eng. Appl. Artif. Intell. 162, 112382. https://doi.org/10.1016/j.engappai.2025.112382.

Yang, L.-J., Wang, Z.-J., Gao, S.-W., et al., 2019. Magnetic flux leakage image classification method for pipeline weld based on optimized convolution kernel. Neurocomputing 365 (6), 229–238. https://doi.org/10.1016/j.neucom.2019.07.083.

Zhang, S.-Z., Li, H.-M., Zhao, C.-T., 2023. Defect-depth-field algorithm for simulating magnetic flux leakage signals based on discrete magnetic dipole model. NDT E Int. 139, 102939. https://doi.org/10.1016/j.ndteint.2023.102939.

Zhang, C.-S., Bi, J.-P., Lv, Y.-X., et al., 2023. Numerical analysis and experimental research on detection of welding defects in pipelines based on magnetic flux leakage. Petroleum Research 8 (4), 550–560. https://doi.org/10.1016/j.ptlrs.2023.05.013.